Nanoscale

ROYAL SOCIETY OF CHEMISTRY

PAPER

View Article Online
View Journal | View Issue

Cite this: *Nanoscale*, 2025, **17**, 9262

# Design and simulation of mid-wavelength InAs/GaSb type-II superlattice avalanche photodiodes

Xinbo Qi,[a] Xiantong Zheng,*[a] Yuan Liu,*[a] Yulin Feng[a] and Dongliang Zhang*[b]

Published on 12 March 2025. Downloaded on 6/12/2026 6:58:17 PM.

Received 12th November 2024, Accepted 11th March 2025

DOI: 10.1039/d4nr04731a

rsc.li/nanoscale

InAs/GaSb type-II superlattice (T2SL) avalanche photodiodes (APDs) are particularly well-suited for low-light detection and quantum communication due to their enhanced sensitivity. However, their performance is significantly impacted by dark current and breakdown voltage characteristics. Here, we explore the performance of T2SL APDs by analysing the relationship between the structural parameters of the absorption, charge, and multiplication layers, utilizing Silvaco software and the equivalent materials method. To enhance the device's performance, we integrated a high-doping AlAsSb charge layer into the separate absorption and multiplication (SAM) structure, constructing a SACM (separate absorption, charge, and multiplication) architecture. Simulation results show that the optimized SAM APD achieves a penetration voltage of 24.7 V and a breakdown voltage of 36.5 V. Notably, the insertion of the charge layer effectively reduced the device's dark current from $10^{-7}$ to $10^{-9}$ A. At an operating temperature of 300 K, the SACM APD demonstrates a gain of 73.4 with a reverse bias voltage of 35 V, surpassing the performance of the SAM structure. These findings provide critical insights for the design of high-performance mid-wave infrared detectors, highlighting the potential of T2SL-APDs in achieving high gain and low dark current.

## 1. Introduction

Mid-wavelength (MW) infrared detectors have extensive applications in both military and civilian domains.[1,2] The ability to detect weak light signals plays a vital role in various key applications, such as night vision and remote target detection in military settings, as well as environmental monitoring and medical imaging in civilian contexts.[3] Avalanche photodiodes (APDs) leverage internal gain generated through the process of impact ionization, offering superior signal-to-noise ratios compared to PIN photodiodes.[4] The optoelectronic characteristics of this avalanche phenomenon have been widely discussed in light-emitting diodes.[5] This enhanced performance makes APDs widely used devices for weak signal detection, particularly in scenarios where the quality of the detected signal can significantly impact decision-making processes. The performance of APDs is often limited by defects in the material, such as dislocations or interface states, which can cause non-radiative recombination and light emission, leading to noise and reduced avalanche gain efficiency. Furthermore, disorder-induced carrier localization, as seen in low-dimensional materials,[6] can decrease the mobility and lifetime of charge carriers, restricting carrier transport in the avalanche region and weakening the energy accumulation required for avalanche gain. To mitigate these challenges, strategies such as defect passivation, controlled doping, and structural engineering are critical for improving APD performance, particularly in high-frequency, high-sensitivity applications.

Research on MW detectors encompasses various material systems, including HgCdTe (MCT),[7] InSb[8] and type-II superlattices (T2SLs).[9] Among these, MCT is often preferred for MW APDs due to its near-zero *k*-value,[10] defined as $\beta/\alpha$, where $\alpha$ and $\beta$ represent the impact ionization coefficients for electrons and holes, respectively. A lower *k*-value indicates reduced excess noise, theoretically enabling higher performance for APDs.[11] However, MCT APDs require higher mercury composition, which complicates material epitaxy and imposes stricter requirements on material growth quality and device processing, leading to lower yield rates.[12] In contrast, T2SLs have gained significant attention in the field of infrared photodetectors due to the high material uniformity, strong tunability of the bandgap, and established III–V device fabrication technologies.[13–16] These advantages make T2SLs a promising alternative for next-generation infrared applications.

[a]School of Instrument Science and Opto-electronics Engineering, Beijing Information Science and Technology University, Beijing 10096, China. E-mail: zxt1001@bistu.edu.cn, yuan.liu@bistu.edu.cn
[b]North China Research Institute of Electro-Optics, Beijing 100015, China. E-mail: zdllzu2007@163.com



This journal is © The Royal Society of Chemistry 2025

Published on 12 March 2025. Downloaded on 6/12/2026 6:58:17 PM.

The avalanche multiplication process of APD provides gain, but it brings additional excess noise due to the randomness of collision ionization processes. When the electric field is high enough, both electrons and holes can generate additional charge carriers by colliding with the lattice to achieve a multiplicative effect. When the ionization coefficient ratio ($k$ value) of holes to electrons ($\beta/\alpha$) is close to 0, the excess noise is minimized in the case of electron-induced multiplication. The ionization coefficients $\alpha$ and $\beta$ represent the probability or ability of electrons and holes, respectively, to undergo collision ionization under a certain electric field. The high electric field required for avalanche multiplication can lead to strong band-to-band tunneling, resulting in significant dark current. To reduce the tunneling current in avalanche photodiodes, a widely adopted approach is to implement a separate absorption and multiplication (SAM) structure.[17] Using a wide band gap material in the multiplication layer reduces the probability of band-to-band tunneling. Previous studies have identified AlAsSb as a wide bandgap material characterized by low $k$-values,[18] indicating a $k$-value of 0.005 for $AlAs_{0.56}Sb_{0.44}$,[19] and the weakest temperature dependence in terms of the rate of $\alpha$ and $\beta$ variance.[20] Furthermore, as the antimony composition increases, the $k$ value of AlAsSb further decreases due to the increased phonon scattering rates and the larger effective mass of holes, which reduces the $\beta$ value.[21] Due to the high Sb composition (0.916) in AlAsSb, which is lattice-matched with GaSb substrates, the theoretical $k$-value is significantly lower. Consequently, AlAsSb is a promising candidate for the multiplication layer material, with enhanced sensitivity and reduced temperature dependence while sustaining the same operating speed. The epitaxial growth of AlAsSb alloys faces significant challenges in achieving lattice matching with the substrate while minimizing strain, as the required arsenic (As) composition must be precisely controlled to ∼8%. In the As/Sb mixed system, controlling the group V elements is challenging, which can lead to phase separation into inhomogeneous binary or ternary compounds. The large flux of As/Sb further complicates the control of group V elements, increasing the likelihood of phase separation into inhomogeneous binary or ternary compounds. However, previous research has shown that these challenges can be mitigated through a digital alloying approach,[22] employing specific growth sequencing to stabilize the material components and prevent phase separation. Consequently, the proposed structure remains experimentally feasible, bridging the gap between theoretical simulations and practical device fabrication.

In this paper, we systematically model and simulate the layer structure of T2SL MW APD using Silvaco software. By comparing the dark current characteristics of devices with different structures at varying bias voltages, we analyzed the impact of absorption layer thickness and doping levels in different regions on dark current and electric field distribution. This comparison enabled us to determine the optimal model parameters. In addition, the insertion of a charge layer improved the electric field distribution, further enhancing performance.

## 2. Method

Technology Computer-Aided Design (TCAD) simulation software plays a crucial role in the research and development of optoelectronic devices and has been widely used in the simulation of devices made from various materials.[23] Its flexible parameter definition capabilities enable simulations to closely approximate real-world device behavior, providing valuable insights and guidance for future experimental studies. Notably, Silvaco TCAD has been successfully employed in prior studies to simulate superlattice materials and other complex heterostructures. These simulations have demonstrated excellent agreement with experimental results, further validating the feasibility and reliability of this approach for modeling advanced optoelectronic systems.[24,25]

In this study, the performance of T2SL APDs was simulated and analyzed in relation to the structural parameters of the absorber, charge, and multiplication layers using Silvaco software and the equivalent material method. The simulation process using the device simulation software Silvaco is as follows: firstly, the mesh size is divided according to the theoretical design model, considering the thickness and interface of each layer. The mesh density has a direct influence on the device's simulation speed. To enhance simulation accuracy, denser meshes should be set at the interfaces of each epitaxial layer, whereas sparser meshes are appropriate within the epitaxial layers. Subsequently, structural parameters, such as material types and doping concentrations for each layer, are defined to complete device structure modeling. Following this, suitable physical models are chosen for numerical calculation. The computational model for device simulation is based on the Poisson equation, the carrier continuity equation, and the transport equation. Various models are invoked to describe diffusion current, generation–recombination current, tunneling current, and photocurrent. By solving the relevant equations, we analyze the variations in physical quantities of the semiconductor device during operation, aiming to optimize its photoelectric performance. The simulation results are then analyzed to refine the theoretical design. Finally, a structure that meets the design requirements is grown in practice. In the subsequent research, feedback analysis will be conducted through various tests on materials and photoelectric devices, which will further refine the simulation outcomes.

Critical to the simulation methodology is Silvaco's material customization capability, where strategic selection of physical models and parameter optimization fundamentally determines simulation accuracy. The software enables adaptive modification of default material properties to match experimental requirements. Notably, due to inherent limitations in simulating superlattice (SLS) configurations directly, we implemented a homogenized bulk material approximation in the input deck rather than modeling periodic nanoscale layers. This computational strategy required meticulous parameter calibration through iterative verification against established SLS characteristics. Following rigorous parameter validation, we integrated the equivalent optoelectronic properties of the

Published on 12 March 2025. Downloaded on 6/12/2026 6:58:17 PM.

entire superlattice absorber into the SAM-APD architecture for comprehensive device-level simulation. The adopted parameters, as cataloged in Table 1, originate from two principal sources: (1) experimentally verified values from prior studies[26–29] and (2) theoretically derived parameters calculated through band structure analysis and weighted averaging techniques. This equivalent bulk modeling approach has dual advantages: it reduces computational complexity by eliminating the need for explicit simulation of hundreds of SLS periods while maintaining physical fidelity and streamlines result validation through simplified post-processing analysis.

As shown in Fig. 1, the energy band structure of the 8 ML InAs/6 ML GaSb T2SL material was calculated with an 8-band K.P model. It can be seen from Fig. 1(a) that the bandgap of the T2SL is 0.258 eV and the corresponding cutoff wavelength is 4.815 μm. Fig. 1(b) shows the device layer structure diagram simulated in this study. Fig. 1(c) illustrates the band structure of this configuration, including both the conduction band and the valence band. From bottom to top, on the GaSb substrate, there is an n+ GaSb buffer layer, an n+ InAs/GaSb T2SL contact layer, an i-$AlAs_{0.08}Sb_{0.92}$ multiplication layer, followed by an InAs/GaSb T2SL absorption layer and a p+ contact layer, and finally a p-type heavily doped InAs cap layer. The specific epitaxial structure is as follows: the buffer layer is a 0.5 μm thick GaSb region doped to $2 \times 10^{18}$ $cm^{-3}$ using GaTe. Then, a 200 nm thick 8 ML InAs/6 ML GaSb SL layer doped to $1 \times 10^{18}$ $cm^{-3}$ using Si was grown on the buffer layer as the n+ contact layer. The multiplication layer is an AlAsSb ternary alloy with a thickness of $W_m$ μm, lattice-matched to the substrate. The absorber is comprised of a $W_a$ μm thick unintentionally doped 8 ML InAs/6 ML GaSb SL region. The p+ contact layer consists of a 0.2 μm thick 8 ML InAs/6 ML GaSb SL layer with the GaSb layer doped to $2 \times 10^{18}$ $cm^{-3}$ using Be, plus a 0.02 μm thick InAs cap layer doped with the same concentration of Be. Finally, a 150 nm thick layer of Ti/Pt/Au is evaporated onto the top and bottom contact layers to serve as electrodes.

**Table 1** Equivalent parameters of the 8 ML InAs/6 ML GaSb superlattice material

| Parameter | Value |
|---|---|
| Bandgap/eV | 0.258 |
| Electron effective mass ($m_0$) | 0.04 |
| Hole effective mass ($m_0$) | 0.75 |
| Permittivity/F $m^{-1}$ | 15.3 |
| Electron affinity/eV | 4.667 |
| Bandgap at 300 K $eV^{-1}$ | 0.258 |
| Electron mobility at 300 K $cm^{-2} \cdot V^{-1} \cdot s^{-1}$ | 1000 |
| Hole mobility at 300 K $cm^{-2}$ $V^{-1}$ $s^{-1}$ | 500 |

## 3. Simulation results and discussion

### 3.1 SAM APD

The absorption region is the narrow-band-gap material InAs/GaSb, while the multiplication region is the wide-band-gap material $AlAs_{0.08}Sb_{0.92}$, which separates photon absorption from carrier multiplication. To reduce tunneling current, the AlAsSb multiplication layer and absorption layer should be respectively in high and low electric fields. Meanwhile, the electric field in the multiplication region should be high to ensure the occurrence of the avalanche multiplication effect. The electric field distribution of the device is shown in Fig. 2. As shown in Fig. 2(a), while the thickness of the multiplication layer increases from 0.5 μm to 0.8 μm, the corresponding peak electric field intensity decreases from $4.2 \times 10^5$ V $cm^{-1}$ to $3.9 \times 10^5$ V $cm^{-1}$. Furthermore, appropriately increasing the thickness of the multiplication region can help reduce the "dead space" effect,[30] thereby avoiding issues of excessive noise and dark current during the avalanche processes. Fig. 2(b) shows the electric field distribution of the device at different doping concentrations in the multiplication layer. When the doping concentration in the multiplication layer is $1 \times 10^{15}$ $cm^{-3}$, the electric field distribution inside the multiplication region of the device is relatively uniform and the electric field is $4.1 \times 10^5$ V $cm^{-1}$. With the increase of the doping concentration in the multiplication layer, the peak electric field intensity increases, causing the distribution to be more inclined, result-

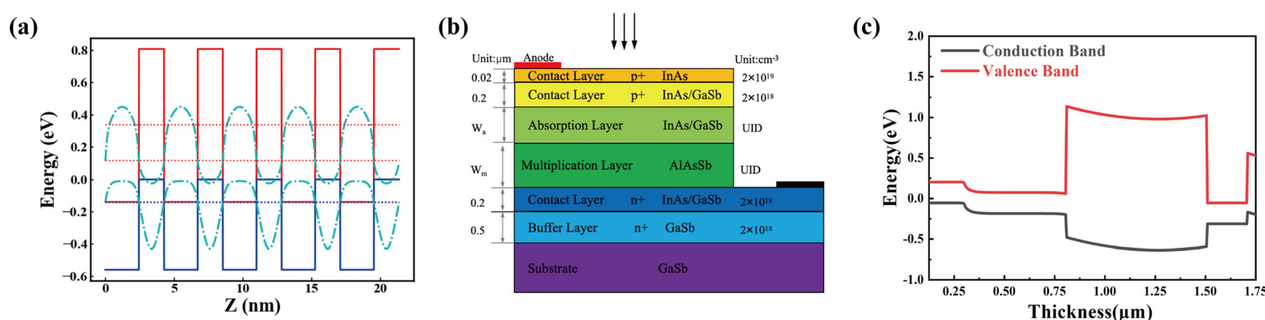


**Fig. 1** (a) Energy band structure of the 8 ML InAs/6 ML GaSb mid-wave superlattice, showing the conduction and valence bands across the material structure, indicating the periodicity of the superlattice and the resulting band alignment. (b) Diagram of the MW T2Sl-APD layer structure, including the contact layers, absorption layers (InAs/GaSb), multiplication layer (AlAsSb), and buffer layer, along with doping concentrations and their respective positions in the device structure; (c) energy band diagram of the SAM-APD device shown in (b), where the black line delineates the conduction band whereas the red line represents the valence band.

 This journal is © The Royal Society of Chemistry 2025

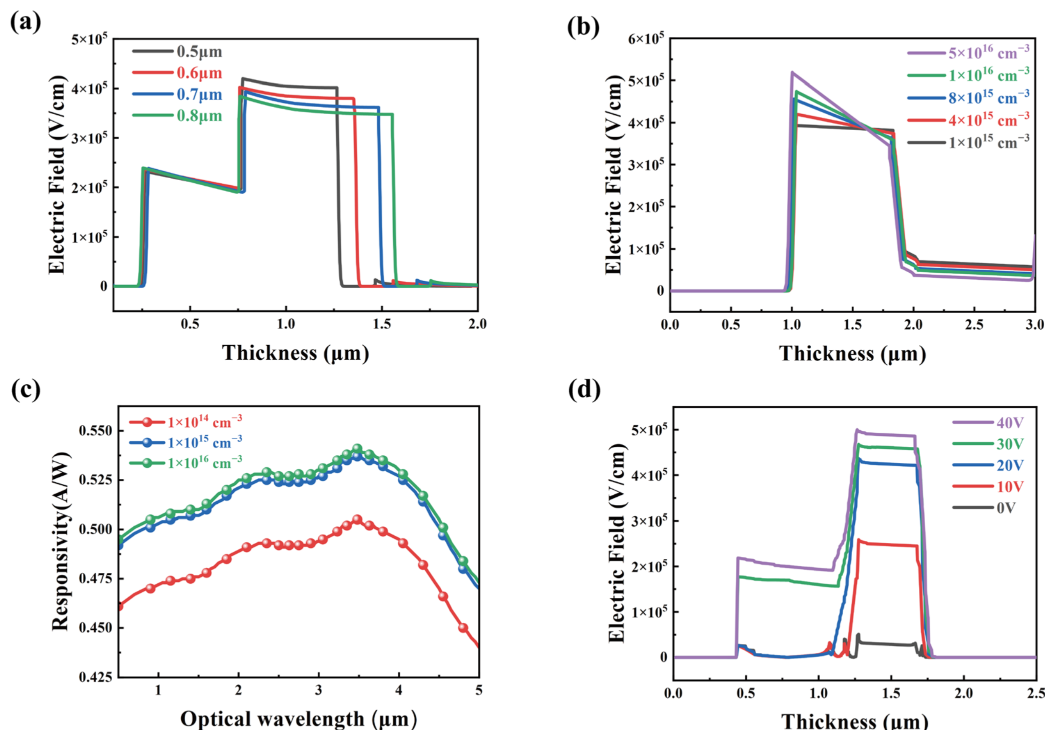


Fig. 2 Electric field distribution of the device: (a) impact of the multiplication layer thickness on the electric field distribution: as the multiplication layer thickness increases from 0.5 μm to 0.8 μm, both the peak position and intensity of the electric field are affected; (b) impact of the doping concentration in the multiplication layer on the electric field distribution; (c) the effect of multiplication layer doping concentration on the optical properties of the device; (d) electric field profile for various reverse bias voltages in a SAM APD.

ing in a nonuniform electric field distribution. When the doping concentration increases to $1 \times 10^{16}$ cm$^{-3}$, the peak electric field strength reaches $5.6 \times 10^5$ V cm$^{-1}$. To ensure a relatively uniform electric field in the multiplication region, reduce noise and enhance gain, the doping concentration of the multiplication region is set to $1 \times 10^{15}$ cm$^{-3}$. Overall, the electric field distribution inside the device can be effectively regulated by analyzing and adjusting the doping concentration and thickness of the multiplication layer. Fig. 2(c) shows the responsivity as a function of optical wavelength, with different multiplication layers. The responsivity peak at around 3.5 μm, with a doping concentration of $1 \times 10^{16}$ cm$^{-3}$, exhibits the highest responsivity. The observed trends can be attributed to the balance between absorption and recombination processes. Higher doping concentrations increase the absorption coefficient, which leads to enhanced responsivity due to more efficient photon absorption.

However, excessive doping also increases the recombination rates, reducing carrier lifetimes and limiting the overall responsivity. The peak positions correspond to the wavelengths where the material achieves maximum absorption efficiency. Fig. 2(d) shows the APD electric field distribution at various bias voltages. At zero bias voltage, the depletion region is formed within the multiplication layer and is part of the absorption layer. As the reverse bias voltage increases, the depletion region extends towards the absorption region. When the bias voltage approaches a certain level, the electron and hole pairs in the APD will accelerate and collide with other atoms due to the high electric field, causing the number of charge carriers to double and resulting in an avalanche effect. This condition is called punch-through, and the corresponding bias voltage is called the punch-through voltage ($V_p$). As the electric field intensity continues to increase, the number of impact ionization events increases sharply, and the multiplication gain $M$ approaches infinity. The corresponding voltage is called the breakdown voltage ($V_b$). Higher $V_p$ and lower $V_b$ values reduce the linear operating range of the APD detector. Conversely, increasing both the breakdown and punch-through voltages complicates the design of the external control circuits and increases system noise.

To enhance the performance and efficiency of the APD, it is essential to optimize the device's linear operating region. Fig. 3 shows the variation trends of $V_p$ and $V_b$ under different thicknesses of the multiplication layer. Fig. 3(a) shows the trend of the $I$–$V$ curves with different multiplication layer thicknesses.

Before the reverse bias voltage reaches the breakdown voltage, the device operates in the linear mode, and the appearance of the breakdown voltage indicates that the photogenerated carriers in the device break through the barrier and reach the multiplication layer. As the reverse bias voltage continues to increase, the photogenerated carriers continue to collide and dissociate in the multiplication layer, and the photocurrent of the device increases slowly. When the bias

Published on 12 March 2025. Downloaded on 6/12/2026 6:58:17 PM.

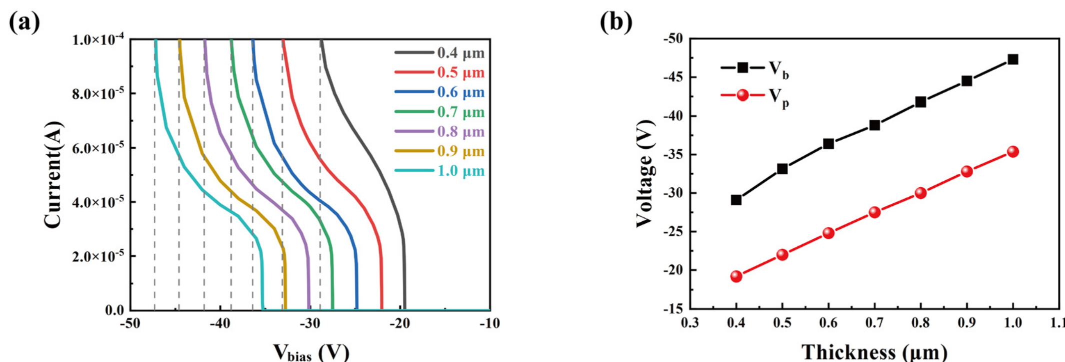


Fig. 3 (a) *I–V* curves of the SAM-APD as a function of the multiplication layer thickness, with the thickness ranging from 0.4 μm to 0.8 μm; (b) the influence of the multiplication layer thickness on the punch-through voltage and breakdown voltage.

Published on 12 March 2025. Downloaded on 6/12/2026 6:58:17 PM.

voltage of the device is close to the breakdown voltage, an avalanche phenomenon occurs in the multiplication region, and the gain of the photocurrent increases rapidly. The detector operates in the Geiger mode at this time. Fig. 3(b) shows the variation in $V_p$ and $V_b$ for various thicknesses of the multiplication layer. The $V_P$ value of the device increases from 19.2 V to 30 V when the thickness of the multiplication layer is increased from 0.4 μm to 1.0 μm. The $V_p$ value increases considerably with the increased width, necessitating a higher external bias to fully deplete the multiplication region. The $V_b$ value of the device increases from 29.1 V to 47.1 V when the thickness of the multiplication layer is increased from 0.4 μm to 1.0 μm. When the multiplication layer thickness is 0.6 μm, the linear operating range of the device is maximized, from 24.7 V to 36.5 V.

### 3.2 SACM APD

According to the design of the SAM structure in the previous section, to optimize the electric field distribution of the device, a layer of p-type highly doped AlAsSb was further introduced as a charge control layer between the absorption region and the multiplication region. The device structure, after adding the charge layer, and the band structure of the SACM device are shown in Fig. 4(a) and (b). By adjusting the width and doping concentration of the charge layer, the electric field distribution of the absorption region and multiplication region can be optimized. Fig. 4(c) and (d) show the regulatory effect of the charge control layer on the electric field distribution. Fig. 4(c) shows that at a bias voltage of 30 V, the insertion of a thin, highly doped charge layer reduces the peak electric field in the absorber region from $2.4 \times 10^5$ V cm$^{-1}$ to $1.1 \times 10^5$ V cm$^{-1}$, while increasing the electric field in the multiplication region from $4 \times 10^5$ V cm$^{-1}$ to $5.2 \times 10^5$ V cm$^{-1}$. When the thickness of the charge control layer is fixed at 0.04 μm, it can be observed that increasing the doping concentration from $1 \times 10^{17}$ cm$^{-3}$ to $2 \times 10^{18}$ cm$^{-3}$ effectively enhances the electric field strength in the multiplication region. However, this also results in a lower electric field in the absorber region, which is unfavorable for carrier transport. The charge layer should ensure that the absorber region has a sufficient electric field, allowing carriers to enter the multiplication region at their saturation velocity for ionization by collision. Therefore, selecting an appropriate doping concentration for the charge layer can effectively increase the overall strength of the electric field in the multiplication region, improve electron transport efficiency, and reduce excess noise.

Fig. 5 shows the *I–V* characteristics and gain curves of SAM APD and SACM APD under no illumination and with a light intensity of 8 W cm$^{-2}$. When the applied bias voltage increases from 0 V to 35 V, the corresponding photocurrent increases from $10^{-11}$ A to $10^{-5}$ A. After the bias voltage reaches approximately 24.7 V, the photocurrent of the SAM APD starts to significantly exceed the dark current, indicating that the photo-generated carriers have overcome the potential barrier and entered the multiplication region. As the bias voltage continues to increase to 36.5 V, the photocurrent and dark current approach each other again. The results show that the SAM APD device's $V_p$ value is approximately 24.7 V, and the $V_b$ value is approximately 36.5 V. Before reaching the punch-through voltage, the absorber region is not fully depleted, and the internal electric field of the device is relatively low at small bias voltages. As a result, carriers cannot gain sufficient energy to reach the multiplication region, and the impact ionization effect is weak, resulting in almost zero gain. In the voltage range from 24.7 V to 36.5 V, the device operates in the linear mode. During this range, photo-generated carriers undergo impact ionization in the multiplication layer, which leads to avalanche multiplication. This process causes the photocurrent to increase in a step-like manner, resulting in a significant increase in gain. When the bias voltage reaches 36.5 V, the current gain increases rapidly, and the device enters the Geiger mode. At a bias voltage of 35 V, the gain of the SAM device reaches 30.6.

After inserting the charge layer, the operating range of the device expands from 20 V to 36.5 V, and the dark current significantly decreases from $10^{-7}$ A to $10^{-9}$ A. At a working voltage of 35 V, the gain increases from 30.6 to 73.4 at 300 K. The dark current density under these typical operating conditions is 5.4 mA cm$^{-2}$. These results indicate that the SACM

 This journal is © The Royal Society of Chemistry 2025

Published on 12 March 2025. Downloaded on 6/12/2026 6:58:17 PM.

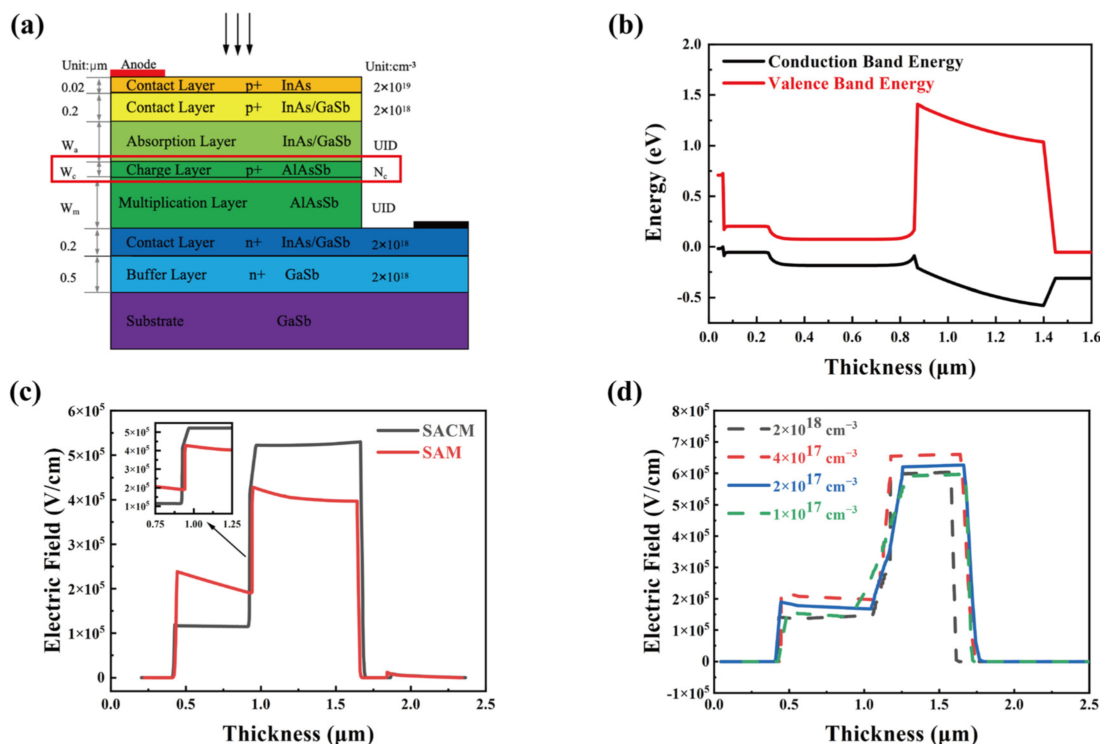


**Fig. 4** (a) Schematic cross-section of the SACM APD structure, illustrating the epitaxial layers (contact, absorption, charge, multiplication, and buffer layers) with material compositions, doping concentrations, and layer thicknesses. (b) Simulated energy band diagram of the SACM-APD: conduction band (black line) and valence band (red line) profiles across the heterostructure. (c) Comparison of electric field distributions in SAM and SACM APDs under identical bias. (d) Electric field profiles in the SACM-APD for varying doping concentrations in the AlAsSb charge layer, highlighting peak field modulation in the multiplication region.

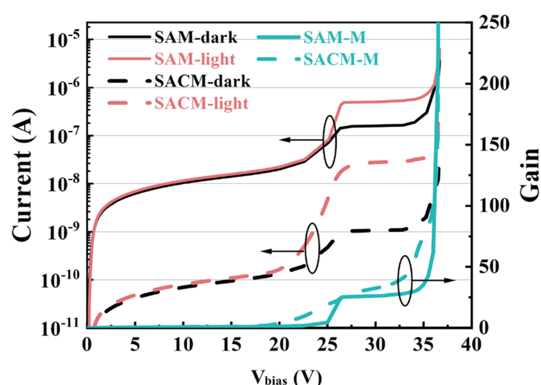


**Fig. 5** The *I*–*V* characteristics and gain curves of SAM and SACM APDs.

device shows significant changes in both current and gain characteristics at different bias voltages. In particular, in the range between the punch-through voltage and breakdown voltage, the gain of the photocurrent increases substantially, indicating that the device has excellent optoelectronic performance.

The comparative analysis of key APD performance metrics (Table 2) highlights the distinct advantages of InAs/GaSb T2SL for MWIR applications under room-temperature operation. The MCT APD exhibits an exceptional multiplication gain ($M$ = 350 @ −9.8 V) at 77 K, attributed to alloy disorder-induced scattering that prolongs carrier dwell time in the multiplication layer, thereby enhancing the impact ionization efficiency. However, MCT suffers severe performance degradation at 300 K, with the dark current density ($J_{dark}$) escalating

**Table 2** Comparison of the key performance parameters of the T2SL-APD and others under specified temperature and bias conditions

| | Ref. | $\lambda_c$ (μm) | $J_{dark}$ (mA $cm^{-2}$) | $V_b$ (V) | $M$ |
|---|---|---|---|---|---|
| InAs/GaSb T2SL | This work | 4.815 μm @ 300 K | 5.4 @ −35 V | −35 | 73.4 @ −35 V |
| MCT($Hg_{0.7}Cd_{0.3}Te$) | 7 | 4.8 μm @ 77 K | ~$10^{-6}$ @ −10 V | −12 | 350 @ −9.8 V |
| | 31 | 3–5 μm @ 300 K | ~10 @ −0.2 V | — | <10 @ −6 V |
| InSb | 8 | 5.4 μm @ 77 K | $3.2 \times 10^{-5}$ @ −50 mV | −4 | 3 @ −4 V |
| InAsSb | 32 | 5.0 μm @ 200 K | $6.6 \times 10^{-3}$ @ −0.9 V | −15 | 29 @ −14.7 V |
| AlInAsSb | 33 | SWIR @ 300 K | 14.1 @ −34 V | −64 | 200 @ −60.8 V |

Published on 12 March 2025. Downloaded on 6/12/2026 6:58:17 PM.

by three orders of magnitude, alongside a collapse in the operational bias range and gain ($M$ < 10 @ −6 V). This degradation stems from thermally activated defects, reduced carrier mobility, and hole accumulation effects, compounded by inherent challenges in achieving high-yield, uniform MCT epitaxy due to Hg instability and Te segregation. The InSb-based APD, while achieving a moderate $J_{dark}$ value ($3.2 \times 10^{-5}$ mA cm$^{-2}$ @ −50 mV), is fundamentally constrained by its narrow bandgap (0.17 eV) and low electron effective mass, which induce significant band-to-band tunneling currents. These limitations restrict the operational bias ($V_b$ < −4 V) and maximum gain ($M$ = 3), rendering it impractical for high-sensitivity MWIR applications. The InAsSb APD partially addresses these issues by extending the cutoff wavelength and improving gain ($M$ = 29 @ −14.7 V), yet the performance remains suboptimal due to residual tunneling currents and temperature-dependent leakage.

In contrast, the InAs/GaSb T2SL APD achieves a balanced performance profile at 300 K: its $J_{dark}$ value (5.4 mA cm$^{-2}$ @ −35 V) is reduced by 191% compared to room-temperature MCT detectors while delivering a competitive gain ($M$ = 73.4 @ −35 V) and extended cutoff wavelength. This stems from T2SL's spatially separated electron–hole wavefunctions, suppressed Auger recombination, and tunable band alignment, which mitigate tunneling currents and enhance carrier lifetime. Notably, AlInAsSb quaternary alloy APDs demonstrate superior gain but are currently limited to short-wave infrared (SWIR) applications, lacking spectral compatibility with MWIR systems. To bridge this gap, future work will explore hybrid architectures integrating T2SL absorbers with optimized AlInAsSb multiplication layers, aiming to synergize T2SL's low-dark-current characteristics with AlInAsSb's high-gain scalability for next-generation MWIR photodetection.

## 4. Conclusions

This study systematically designs and simulates mid-wavelength avalanche photodiodes based on InAs/GaSb T2SLs, with a focus on optimizing the absorption, charge, and multiplication region to discuss the impact of dark current and breakdown voltage on APD performance. Simulation results show that the optimized SACM-APD has a $V_p$ value of 20 V and a $V_b$ value of 36.5 V, demonstrating excellent electric field distribution and gain characteristics. The thickness and doping concentration of the multiplication layer significantly affect the electric field distribution and device performance. Increasing the width of the multiplication region results in a linear increase in $V_p$, while $V_b$ exhibits a nonlinear trend, initially decreasing and then increasing. By inserting the charge layer, the electric field distribution in both the absorption and multiplication regions is effectively optimized, which reduces dark current and enhances gain. At a bias voltage of 35 V, the optimized SACM APD achieves a gain of 73.4, significantly higher than that of the traditional SAM APD, with a notable increase in gain within the punch-through and breakdown voltage ranges.

Through detailed simulation analysis, this research proposes effective structural optimization methods, providing valuable references for the design and fabrication of high-performance mid-wavelength avalanche photodiodes. Future research could further explore other material systems and structural optimization strategies to further enhance APD performance.

## Data availability

Data underpinning the figures that support this work are available within the paper.

## Conflicts of interest

There are no conflicts to declare.

## Acknowledgements

This work was also supported by funding from the National Natural Science Foundation of China (NSFC) (62105039) and the Young Elite Scientist Sponsorship Program by the China Association for Science and Technology (grant no. YESS20200146).

## References

1 J. Chen, J. Wang, X. Li, J. Chen, F. Yu, J. He, J. Wang, Z. Zhao, G. Li and X. Chen, *Sensors*, 2022, **22**(2), 677.
2 C. Coffey, *Opt. Photonics News*, 2011, **22**(4), 26–31.
3 S. Gunapala, S. Keo, D. Z. Ting and A. Soibel, *Infrared Phys. Technol.*, 2019, **96**, 251–261.
4 O. Kharraz and D. Forsyth, *Optik*, 2013, **124**(13), 1493–1498.
5 Y. Chen, D. Xu, K. Xu, N. Zhang and W. S. Jacobus, *Chin. Phys. B*, 2019, **28**(10), 107801.
6 A. Cresti, N. Nemec, B. Biel, G. Niebler, F. Triozon, G. Cuniberti and S. Roche, *Nano Res.*, 2008, **1**(5), 361–394.
7 R. J. Gu, C. Shen, W. Q. Wang, X. L. Fu and L. Chen, *J. Infrared Millimeter Waves*, 2013, **32**(2), 136.
8 J. Abautret, J. P. Perez, A. Evirgen, J. Rothman, A. Cordat and P. Christol, *J. Appl. Phys.*, 2015, **117**(24), 998.
9 S. Lee, A. Kazemi, S. H. Kodati, S. Mathews, T. J. Ronningen, M. Winslow, C. H. Grein, N. Ye, A. H. Jones and J. C. Campbell, *SPIE Defense + Security Conference*, 2018.
10 M. Kopytko, J. Sobieski, W. Gawron and P. Martyniuk, *Sensors*, 2022, **22**(3), 924.
11 F. Capasso, W. T. Tsang, A. L. Hutchinson and G. F. Williams, *Appl. Phys. Lett.*, 1982, **40**(1), 38–40.
12 W. Lei, J. Antoszewski and L. Faraone, *Appl. Phys. Rev.*, 2015, **2**(4), 041303.

 This journal is © The Royal Society of Chemistry 2025

Published on 12 March 2025. Downloaded on 6/12/2026 6:58:17 PM.

13 H. J. Haugan, F. Szmulowicz, G. J. Brown and K. Mahalingam, *J. Appl. Phys.*, 2004, **96**(5), 2580–2585.
14 Y. Yang, X. Zheng, J. Wen, Z. Liu, B. Liu, J. Yu, D. Zhang, Y. Liu, L. Lu, Y. Feng, G. Chen, F. Luo, M. Dong and L. Zhu, *Micro Nanostruct.*, 2023, **178**, 207578.
15 J. Rodriguez, P. Christol, L. Cerutti, F. Chevrier and A. Joullie, *J. Cryst. Growth*, 2005, **274**(1–2), 6–13.
16 J. Wen, X. Zheng, X. Qi, N. Wen, W. Chen, Y. Feng, L. Lu, G. Chen, H. Wang and M. Dong, *Infrared Phys. Technol.*, 2024, **136**, 105075.
17 V. Palenskis, J. Matukas, D. Stučinskas, K. A. Kaminskas, E. Žitkevičius and J. Lithuanian, *J. Phys.*, 2003, **43**(5), 385–390.
18 S. Yan, J. Huang, Y. Zhang and W. Ma, *IEEE Electron Device Lett.*, 2021, **11**, 42.
19 S. Xie and C. H. Tan, *IEEE J. Quantum Electron.*, 2011, **47**(11), 1391–1395.
20 X. Jin, S. Xie, B. Liang, X. Yi, H. Lewis, L. W. Lim, Y. Liu, B. K. Ng, D. L. Huffaker, C. H. Tan, D. S. Ong and P. R. David, *Optical Components and Materials XI*X, 2022, **11997**, 63–73;.
21 S. Z. Ahmed, Y. Tan, J. Zheng, J. C. Campbell and A. W. Ghosh, *Phys. Rev. Appl.*, 2022, **17**(3), 034044.
22 J. Bor-Chau, B. Liang, D. Ren, P. David, C. Arion and H. Diana, *Crystals*, 2017, **7**(10), 313.
23 K. Xu, *J. Micromech. Microeng.*, 2021, **31**(5), 1–10.
24 K. Banerjee, J. Huang and S. Ghosh, *Infrared Phys. Technol.*, 2011, **54**(6), 460–464.
25 A. M. Laoufi, B. Dennai, O. Kadi, *et al.*, *Chalcogenide Lett.*, 2021, **18**(6), 297–301.
26 W. J. Li, L. Q. Zhu, D. L. Zhang, X. T. Zheng, Y. C. Yang, W. J. Wang, Y. Liu, L. D. Lu and M. Liu, *Infrared Laser Eng.*, 2023, **52**(9), 20220837.
27 P. F. Qiao, S. Mou and S. L. Chuang, *Opt. Express*, 2012, **20**(3), 2319–2334.
28 E. Steveler, M. Verdun, B. Portier, P. Chevalier, C. Dupuis, N. Bardou, J. B. Rodriguez, R. Haïdar, F. Pardo and J. L. Pelouar, *Appl. Phys. Lett.*, 2014, **105**(14), 141103.
29 M. Delmas, J. Rodriguez and P. Christol, *J. Appl. Phys.*, 2014, **116**(11), 113101–113101.
30 M. A. Khamis, W. E. Rashid, P. J. Ker and K. Y. Lau, *Int. J. Eng. Technol.*, 2018, **7**(4.35), 559–563.
31 L. Zhu, H. Guo, Z. Deng, L. Yang, J. Huang, D. Yang, Z. Zhou, C. Shen, L. Chen, C. Lin and B. Chen, *IEEE J. Sel. Top. Quantum Electron.*, 2022, **28**(2), 1–9.
32 J. Li, A. Dehzangi, G. Brown and M. Razeghi, *Sci. Rep.*, 2021, **11**(1), 7104.
33 Y. Lyu, X. Han, Y. Sun, Z. Jiang, C. Guo, W. Xiang, Y. Dong, J. Cui, Y. Yao and D. Jiang, *J. Cryst. Growth*, 2017, **482**, 70–74.